ISSN: 2663-2187

https://doi.org/ 10.48047/AFJBS.6.9.2024.5490-5505

African Journal of Biological Sciences

Journal homepage: http://www.afjbs.com

Research Paper Open Access

# Influence of Deposition Time Variation on the Structural and Electrochemical Properties of $Fe_2O_3$ Thin Films via SILAR for Supercapacitor Applications

**Sanjaykumar S. Pujari[1], Rushikesh. G. Bobade [2], Mahadev T. Mhetre[3,1], Prathamesh B. Dahivade[1], Swapnil N. Pawar[1], Revanappa. C. Ambare [2,*], Balkrishna. J. Lokhande [1*],**

[1] Lab of Electrochemical Studies, School of Physical Sciences, PAH Solapur University, Solapur, Maharashtra, India.

[2] Department of Physics, KMC, College, Khopoli-410203, Raigad (Affiliated to University of Mumbai), Maharashtra, India.

[3] Santosh Bhimrao Patil Arts, Commerce, and Science College, Mandrup, South Solapur, Solapur, Maharashtra 413221, India

***Corresponding author: Prof. B.J. Lokhande, E-mail address:** bjlokhande@yahoo.com,

**Dr. Revanappa. C. Ambare, Email address:** revanambare@gmail.com

Article History: Volume 6,Issue 9, 2024

Received: 29 Apr 2024

Accepted : 01 Jun 2024

doi:10.48047/AFJBS.6.9.2024.5490-5505

**Abstract**

In this study, we successfully synthesized small granular ferric oxide ($Fe_2O_3$) thin films on stainless steel (SS) using successive ionic layer adsorption and reaction (SILAR) technique. The optimized $Fe_2O_3$ thin films underwent comprehensive physical characterization, revealing a hexagonal structure via X-ray diffraction (XRD). Field Emission Scanning Electron Microscopy (FE-SEM) confirm a small granular morphology. Electrochemical performance was assessed through cyclic voltammetry (CV), galvanostatic charge-discharge (GCD), and electrochemical impedance spectroscopy (EIS). The $Fe_2O_3$ nanograins demonstrated a high specific capacitance (Cs) of 744.7 F/g. Specific energy (SE) and specific power (SP) values peaked at 75.2 Wh/kg and 1.3 kW/kg, respectively, at 1 mA/cm² in a 1M KOH electrolyte. The EIS analysis confirmed an internal resistance (Ri) of 1.4 Ω, indicating excellent power concert and rate ability. These findings underscore the efficacy of the SILAR method in producing high-performance $Fe_2O_3$ nanostructures for supercapacitor applications, offering a cost-effective and scalable approach for energy storage solutions.

**Keywords:** $Fe_2O_3$, Small granular morphology, SILAR, Supercapacitor, Thin film.

## 1. Introduction

The escalating request for sustainable and competent energy device solutions have driven significant research into advanced energy storage devices. Among these, supercapacitors stand out due to their superior power density, fast charge-discharge proficiencies, and long cycle life, construction them ideal for a extensive range of applications, from transferable electronics to grid-scale energy storage and electric vehicles [1][2][3][4]. One of the critical components influential the performance of supercapacitors is an electrode material. In this context, ferric oxide ($Fe_2O_3$) has emerged as a highly promising candidate. Ferric oxide, commonly known as hematite, is an iron oxide that offers several advantages for supercapacitor applications. It is abundantly available, environmentally friendly, and cost-effective, which makes it suitable for scalable production. $Fe_2O_3$ possesses a high theoretical capacitance due to its multiple oxidation states, enabling it to undergo various redox reactions essential for charge storage and release. Additionally, $Fe_2O_3$ exhibits good chemical stability and can be engineered into various nanostructures, which significantly enhance its electrochemical properties via increasing an active surface area and facilitating efficient electron transport [2][3][5][6][7][8].

In this study, we employed the SILAR method to manufacture $Fe_2O_3$ thin films, focusing on the effects of varying the deposition (or "deepening") time on their structural and electrochemical properties. The SILAR technique is advantageous for the deposition of thin films due to its simplicity, low cost, and accurate control over film thickness and alignment [9][10][11][12][13][14]. This method involves the alternate involvement of a substrate into solutions containing cationic and anionic solution, allowing for the gradual build-up of the desired material layer by layer. By varying the immersion times in each precursor solution, we can systematically study and optimize the growth conditions to achieve the best possible performance for supercapacitor. The prime goal of this research has to understand how changes in deepening time during the SILAR process influence the crystallinity, morphology, and electrochemical behavior of $Fe_2O_3$ thin films. Comprehensive physical characterization was performed using XRD to identify the crystallographic structure of a films, which revealed a well-defined cubic phase characteristic of high-quality $Fe_2O_3$ [15][16][17][18]. FE-SEM was utilized to examine a surface morphology, showing granular structures that provide a high surface area, crucial for enhancing electrochemical activity.

In the present investigation, the $Fe_2O_3$ film was manufactured by SILAR technique, since a SILAR technique was used to synthesize a uniform film at room temperature. A present study rumors on a synthesis of a small grain like network of $Fe_2O_3$ film on SS substrate by a simple and low-cost SILAR technique. Using XRD, FE-SEM, and EDAX, the structural, morphological, and electrochemical characteristics of a deposited films were examined.

## 2. Experimental

### *2.1 Materials*

Ferric nitrate formula [$Fe(NO_3)_3$] (99% extra pure). sodium hydroxide pallets [NaOH] (98% extra pure), hydrochloric acid [HCl], and acetone. All chemicals bought from SDFCL chemical Ltd. All chemicals were used without using extra purification. Stainless steel (SS) was used as a conducting working electrode.

### *2.2 Substrate Cleaning*

The SS substrate was primarily polished by polish paper and then rinsed in distilled water (DW), ultrasonicated in an acetone solution for 30-40 minutes, and dried in an oven at 333 K. After being repeatedly ultrasonicated in a 10 % HCl solution for 10 minutes, they were frequently cleaned with DW. An airtight container was utilized to store all of a ready substrates for use throughout the synthesis [10].

### *2.3 Synthesis of $Fe_2O_3$ thin film electrode*

We synthesized $Fe_2O_3$ thin films using the SILAR method, with a specific focus on varying dipping times to determine their impact on the film properties. The cation solution used was 0.2 M $Fe(NO_3)_3$, and the anion solution was 0.2 M NaOH. The deposition process involved 50 cycles of immersion, utilizing a four-beaker setup that included sequential dipping into the cation solution ($Fe^{3+}$ ions), distilled water, the anion solution ($OH^-$ ions), and another distilled water rinse. We varied the immersion times among three different sets: 20-10-20-10 seconds (DF1), 30-10-30-10 seconds (DF2), and 40-10-40-10 seconds (DF3), where the first and third values correspond to the dipping times in the cation and anion solutions, respectively, and the second and fourth values correspond to the dipping times in the distilled water rinses. Following the deposition cycles, the films were calcined at 623K to promote crystallization and ensure the formation of $Fe_2O_3$. This methodological variation allowed us to systematically investigate the influence of dipping time on the structural and morphological characteristics of the synthesized $Fe_2O_3$ thin films [10][9].

### *2.4 Electrochemical measurements*

To estimate electrochemical properties, we utilized CV, GCD, and EIS with an HCH 600D SPL electrochemical analyzer. A standard three-electrode setup had employed, using a 1 M KOH solution as the electrolyte. A working electrodes were a $Fe_2O_3$ electrode, the counter electrodes were a platinum wire, and an Ag/AgCl as a reference electrode. CV measurements were conducted at scan rates from 5 to 100 mV/s within a voltage window of -1.47 to 0.0 V. CP measurements was carried out at current densities from 1 to 5 mA/cm² at a constant potential of 1.47 V. The specific capacitance (Cs) of the materials was calculated using the appropriate formula for these measurements [10][9].

$$C_s = \frac{1}{mv\,(v_f - v_i)} \int_{v_i}^{v_f} I\,(V)\,dv \quad (1)$$

$$SE = \frac{V \times I_d \times t_d}{m} \quad (2)$$

$$SP = \frac{V \times I_d}{m} \quad (3)$$

$$\eta\,(\%) = \frac{t_d}{t_d} \times 100 \quad (4)$$

Where ($V_f$ - $V_i$) potential window, ‘m’ active mass on an electrode, ‘v’ sweep rate in mV/s, ‘I (V)’ current in mA, ‘$I_d$’ discharge current, and ‘$t_c$’ charging time in sec., ‘$t_d$’ discharge time in sec.

### *2.5 Characterization details*

The crystal structure with plane orientations of the samples were resolute using XRD analysis with a Rigaku D/max 2550 Vb+/PC diffractometer, utilizing Cu Kα radiation (λ = 1.5406 Å). A microstructure was examined using a Hitachi S-4800 FE-SEM operating at 15 kV. Wettability studies of the fabricated electrodes were conducted using a Holmark HO-IAD-CAN-01 apparatus. The weight of the deposited material had measured with a high-precision systematic microbalance (Tapson's-100 TS) using the weight difference method.

Electrochemical properties of $Fe_2O_3$ film electrodes were evaluated in a three-electrode setup using a computer-controlled potentiostat (HCH 600D SPL electrochemical analyzer/workstation). In this setup, a saturated Ag/AgCl electrode served as the reference, a platinum wire as the counter electrode, and the working electrode was a $Fe_2O_3$ film (1.5×1.5 $cm^2$) immersed in the electrolyte. Cyclic voltammetry (CV) plots were obtained to calculate the specific capacitance (Cs). Charge-discharge characteristics were studied using galvanostatic charge-discharge (GCD) at different current densities to calculate specific energy (SE) and specific power (SP). The EIS was performed with an AC signal over a frequency range of 100 Hz to 1 MHz to evaluate the internal resistance of a supercapacitor.

## 3. Results and discussion

### *3.1 Reaction kinetics*

We synthesized $Fe_2O_3$ electrode using the SILAR method, employing 0.2 M $Fe(NO_3)_3$ as the cation source and 0.2 M NaOH as the anion source. During each cycle, $Fe^{3+}$ ions adsorbed onto the substrate react with $OH^-$ ions to form $Fe(OH)_3$, which is converted to $Fe_2O_3$ upon calcination. The repeated immersion and rinsing ensure the formation of a uniform and pure $Fe_2O_3$ film, with the dipping time optimization enhancing the film's crystallinity and uniformity [19][20]:

$$Fe(NO_3)_3 \longrightarrow Fe^{3+} + 3NO_3^- \quad (5)$$

$$NaOH \longrightarrow Na^+ + OH^- \quad (6)$$

$$Fe^{3+} + OH^- \longrightarrow Fe(OH)_3 \quad (7)$$

$$2Fe(OH)_3 \xrightarrow{(673\ K)} Fe_2O_3 + 3H_2O \uparrow \quad (8)$$

The final optimized electrode of $Fe_2O_3$ used for dissimilar physical and chemical characterization methods.

### *3.2 Structural analysis*

The X-ray diffraction (XRD) analysis depicted in **Fig. 1** showcases the patterns of pure $Fe_2O_3$ thin films deposited on stainless steel (SS) substrates. Remarkably, the observed d-spacing values precisely matched the standard d-values extracted from the JCPDS data card No. 33-0664 for $Fe_2O_3$. Evidently, distinct peaks emerged at angles 2θ = 43.4°, 44.4°, 50.6°, 64.4°, 74.4°, and 81.9°, corresponding to crystal planes (113), (202), (024), (300), (220), and (015), respectively. This alignment unequivocally confirms hexagonal crystal structure of $Fe_2O_3$. Notably, the intensity of the peak at 2θ = 44.4° (202) significantly stands out, indicative of a highly crystalline structure. Such pronounced intensity underscores the well-ordered arrangement of atoms or molecules within the $Fe_2O_3$ lattice, characteristic of crystalline materials. Consistent with prior findings by Xia *et al.* [21], these results reaffirm the hexagonal crystal structure of $Fe_2O_3$ nanoparticles. Moreover, the absence of additional phase peaks signifies complete conversion of the deposited hydroxide into $Fe_2O_3$. By applying Scherrer's equation [22], the crystallite sizes (D) were estimated, revealing average sizes of around 56.3 nm, 39.1 nm, and 42.8 nm for samples DF1, DF2, and DF3, respectively. These findings underscore the successful synthesis of highly crystalline $Fe_2O_3$ thin films, demonstrating distinct crystallite sizes attributed to variations in the SILAR method's dipping times.

$$D = \frac{K\lambda}{\beta\ cos\theta} \quad (9)$$

Where, 'K' constant (0.9), 'λ' wavelength of X-ray, 'β' full-width half maximum (FWHM), and 'θ' Braggs angle.

The following formula was used to determine the microstrain: Eq. (10).

$$\varepsilon = \frac{\beta}{4\tan\theta} \quad (10)$$

The intended value of the micro-strain of samples DF1, DF2, and DF3 was 0.0328, 0.0592, 0.0443 respectively.

The subsequent formula was used to regulate the dislocation density: Eq. (11)

$$\delta = \frac{1}{D^2} \quad (11)$$

The intended value of a dislocation density [23] of $Fe_2O_3$ was 3.49, 5.39, 4.51, of DF1, DF2, and DF3 respectively shown in **Table 1**.

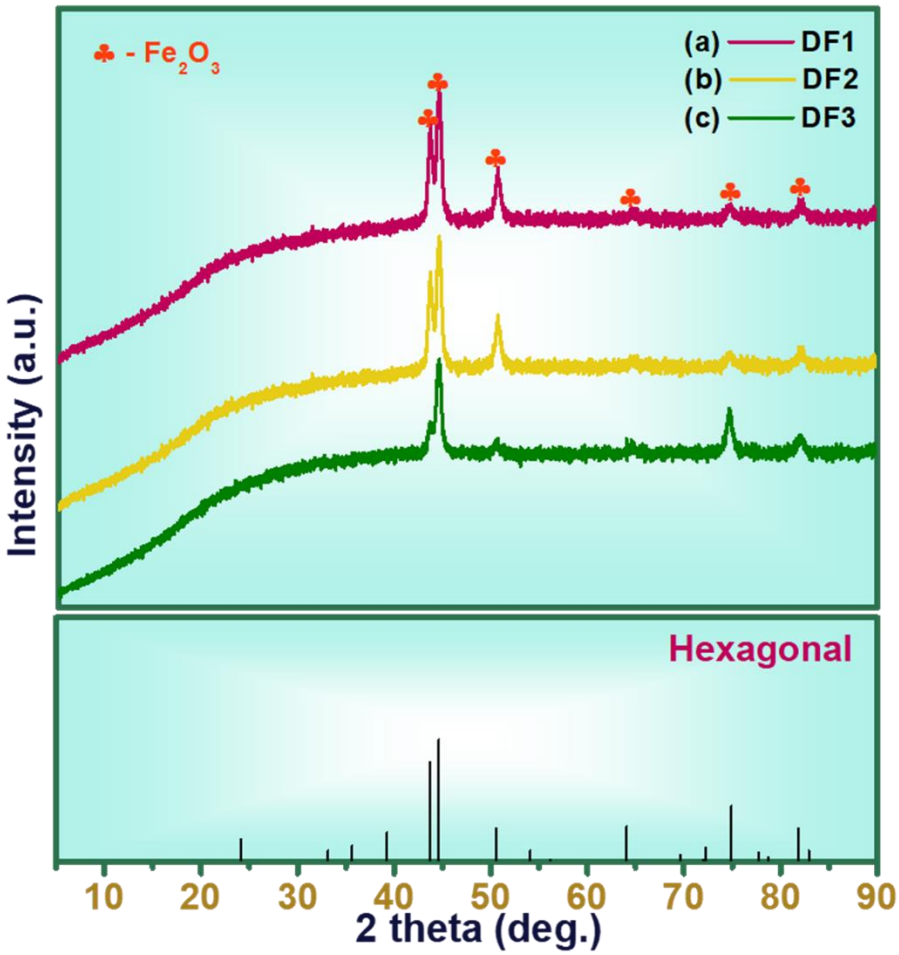


**Fig 1**: XRD plots of sample **(a)** DF1, **(b)** DF2, and **(c)** DF3

| Sample code | Crystallite size (D) (nm) | Micro strain (ε) ($10^{-3}$) | Dislocation density (δ) (× $10^{15}$) lines $m^{-2}$ |
|---|---|---|---|
| **DF1** | 56.3 | 0.0328 | 3.49 |

| | | | |
|---|---|---|---|
| **DF2** | 39.1 | 0.0592 | 5.39 |
| **DF3** | 42.8 | 0.0443 | 4.51 |

**Table 1:** Structural variation of DF1, DF2, and DF3 electrode in terms of crystalline size, micro strain, and dislocation density.

***3.3 FE-SEM and EDAX analysis***

**Fig 2 (a-f)** illustration the FE-SEM images of sample DF2 and DF3 by adjusting the immersion times in each solution, we created two distinct samples designated DF2 and DF3 each with different cycle variations. Upon FE-SEM imaging at magnifications of 10 μm and 1 μm, we observed a granular morphology consistent across all samples, indicative of small grain-like structures. Notably, the higher resolution 1 μm images provided finer details of the grain structure similar result reported by Nehru *et al.* [24]. Further analysis revealed sample DF3 to possess the smallest grain size at 42.6 nm, while DF2 exhibited a slightly larger grain size of 46.2 nm. These findings underscore the significant effect of deposition cycle variations on the morphology and grain size of $Fe_2O_3$. The observed grain-like morphology suggests the potential for enhanced surface area and reactivity, crucial factors for numerous applications. Understanding and controlling the grain size and morphology of $Fe_2O_3$ thin films hold promise for tailoring their properties to specific applications, offering avenues for further research and development in nanomaterials synthesis and engineering. In **Fig. 3 (a)**, the presence of chemical elements crucial for $Fe_2O_3$, notably Fe and O, was verified through Energy Dispersive X-ray Analysis (EDAX). The substantial composition analysis yielded weight percentages of 96.08% for Fe and 3.92% for O, indicating the predominant presence of iron oxide in the synthesized nanomaterials. Additionally, the atomic percentages of Fe and O were determined to be 87.53% and 12.47%, respectively, reaffirming the elemental composition consistent with $Fe_2O_3$. Further insights into the elemental distribution and spatial arrangement were obtained through elemental mapping analysis, as illustrated in **Fig. 3 (b-d)** for the DF2 sample. The elemental mapping images clearly depict the occurrence of Fe and O throughout a sample, confirming the homogeneous distribution of these chemical elements. The utilization of EDAX mapping enabled a comprehensive understanding of the chemical composition and distribution of $Fe_2O_3$ nanomaterials, validating their suitability for various applications in catalysis, sensing, and energy storage.

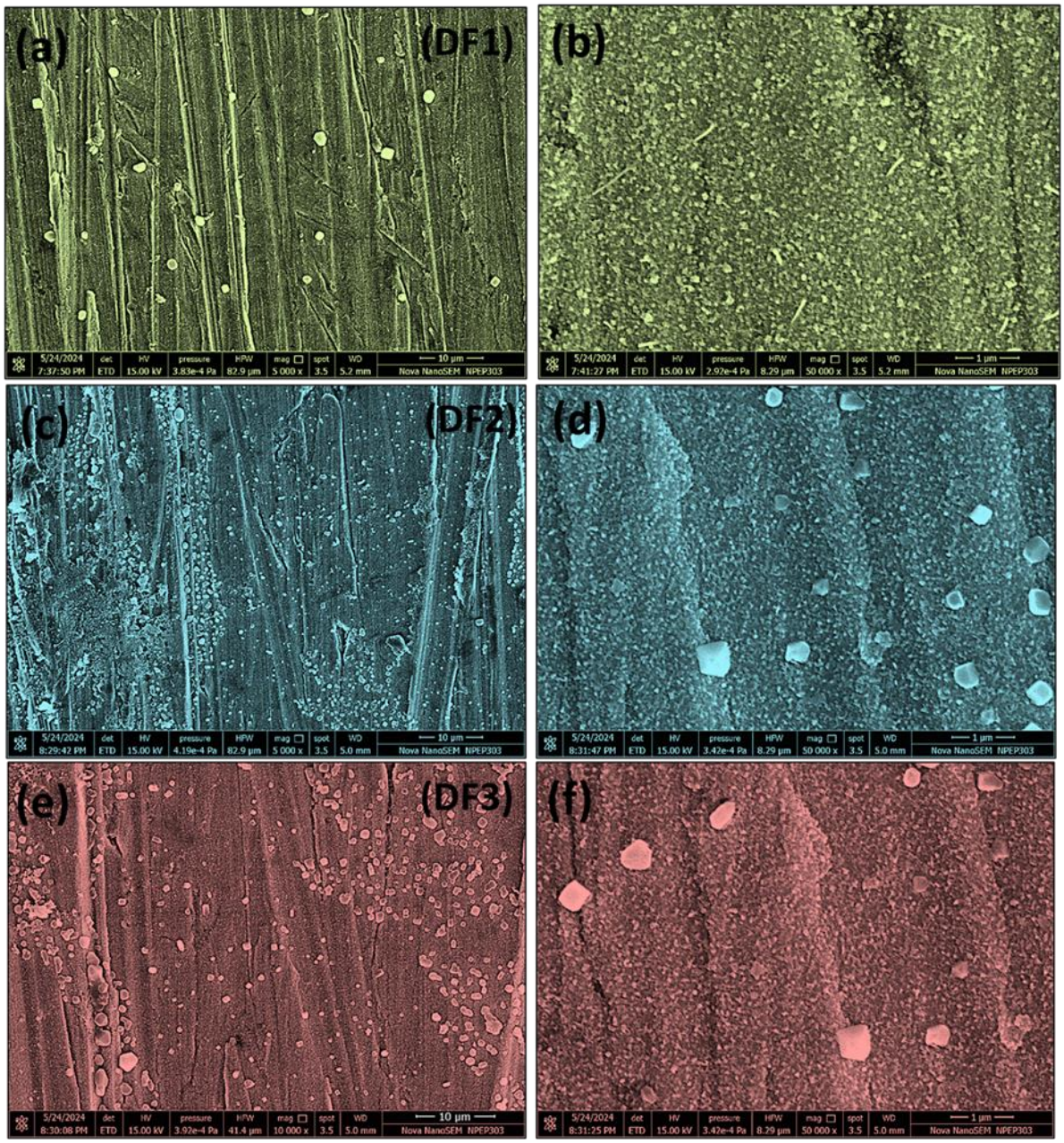


**Fig 2:** FE-SEM images of typical samples **(a-b)** DF1, **(c-d)** DF2, **(e-f)** DF3.

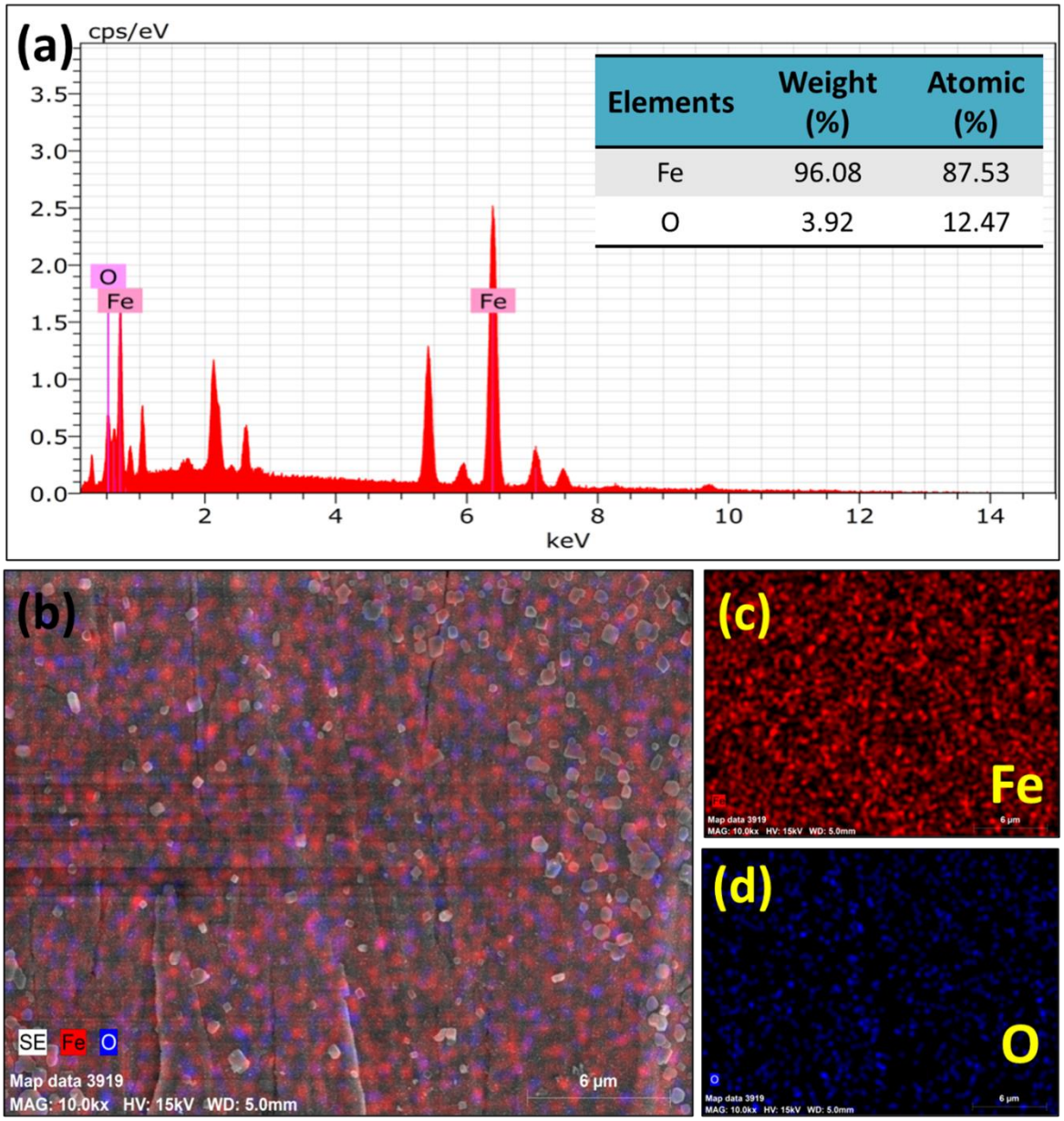


**Fig 3: (a)** EDAX spectrum with percentage of chemical elements present in DF2 electrode, **(b)** The EDAX mapping image of DF2 electrode, and **(c-d)** Elemental mapping images showing the individual distribution of Fe, and O.

***3.4 Wettability study***

The wettability of $Fe_2O_3$ thin films synthesized via the SILAR method was investigated through contact angle measurements. Varying the immersion times during deposition resulted in three distinct samples. The contact angle measurements revealed differences in wettability among the samples, with contact angles of 80.7°, 78°, and 93° observed for DF1, DF2, and DF3, respectively show in **Fig 4 (a-c)**. The contact angle serves as a crucial indicator of surface hydrophobicity or hydrophilicity, with smaller contact angles indicating higher hydrophilicity and larger angles suggesting greater hydrophobicity. The observed contact angles suggest that sample DF1 exhibits the highest hydrophilicity, followed by DF2, while DF3 demonstrates the highest degree of hydrophobicity among the samples. These findings offer valuable insights into the surface properties of $Fe_2O_3$ thin films,

which are essential for various applications. The variation in contact angles among the samples underscores the significance of deposition parameters in tailoring surface properties.

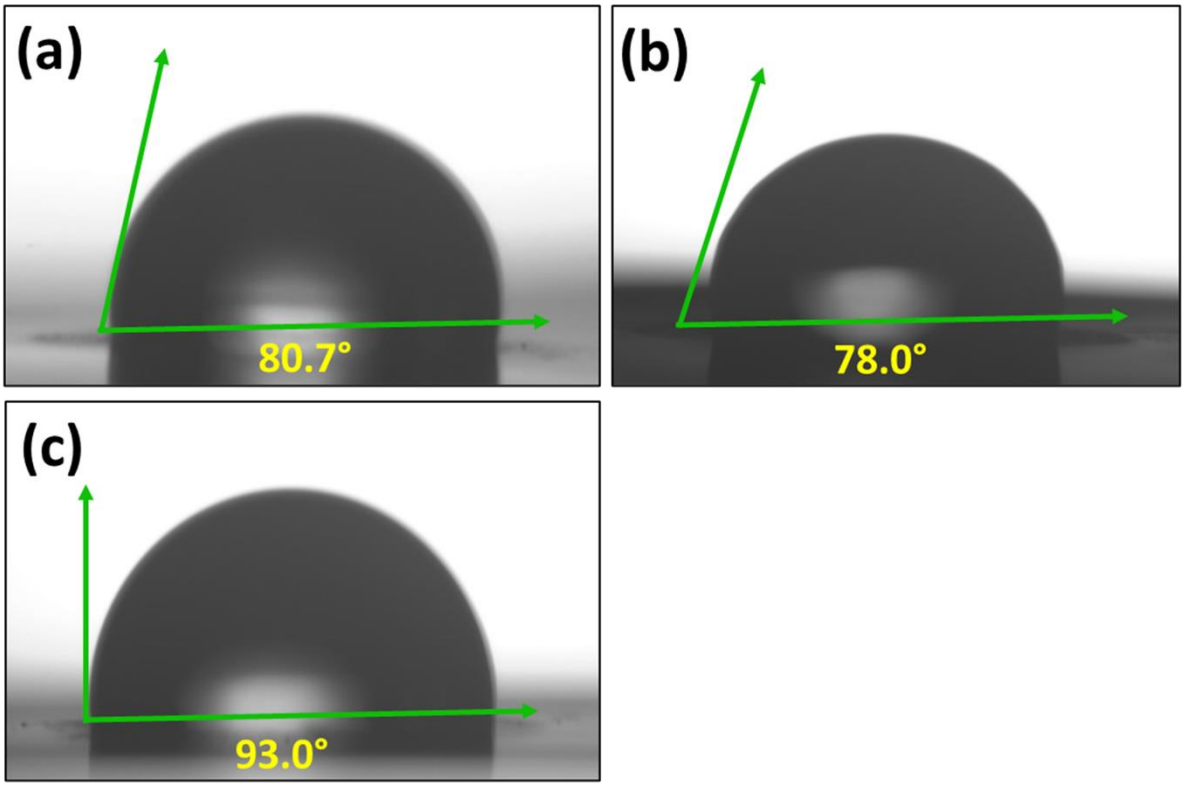


**Fig 4:** Contact angle of sample **(a)** DF1**, (b)** DF2**, (c)** DF3.

***3.5 Electrochemical analysis***

***3.5.1 Cyclic voltammetry analysis***

In our investigation $Fe_2O_3$ thin film was synthesized using SILAR method, with variations in deposition cycles resulting in distinct morphologies and electrochemical properties. Samples DF1, DF2, and DF3, corresponding to different immersion time variations show in **Fig. 5 (a)**. Through CV analysis, DF2 demonstrated the highest Cs of 744.7 F/g at a sweep rate of 5 mV/s in 1 M KOH electrolyte, surpassing DF1 and DF3 with specific capacitances of 520.8 and 512 F/g, respectively show in **Fig. 5 (b)**. This enhancement in Cs of DF2 can be attributed to its finer grain size, higher crystallinity, and improved wettability angle, reflecting enhanced electrode-electrolyte interactions. Furthermore, the potential window for these measurements ranged from -1.47 to 0 V vs Ag/AgCl, providing insights into the electrochemical stability of $Fe_2O_3$ thin film electrodes [1][5]. These findings underscore the significant impact of deposition constraints on both a morphological and electrochemical properties of $Fe_2O_3$ electrode, holding promise for their application in advanced energy devices. **Table 2** show the variation of Cs in F/g at sweep rate of 5 mV/s for dissimilar electrode (DF1, DF2, DF3).

The optimization achieved through Deeping time variation resulting in the final electrode denoted as DF2. To comprehensively assess the electrochemical performance of DF2, CV analyses were conducted at various sweep rates ranging from 5 to 100 mV/s in 1 M KOH electrolyte show in **Fig. 5 (c)**. Notably, DF2 exhibited specific capacitance values of 744.7, 663.5, 661.7, 650.6, and 645.3 F/g at sweep rates of 5-100 mV/s, respectively show in

**Fig. 5 (d)**. and all data summarized in **Table 3**. These results underscore the remarkable capacitance retention of DF2 across a wide range of scan rates, indicative of its excellent charge storage capability and electrochemical permanency. Additionally, a potential window for these measurements spanned from -1.47 to 0 V vs Ag/AgCl, highlighting an electrochemical stability of a $Fe_2O_3$ thin film electrode. The observed trends in specific capacitance with varying scan rates provide valuable insights into the charge storage mechanisms and kinetics of DF2 [10][19], essential for its application in energy storage devices and electrochemical systems requiring high performance and reliability. **Table 4** show the evaluation of electrochemical characteristics of $Fe_2O_3$ by other described other metal oxide-based thin film in aqueous electrolyte

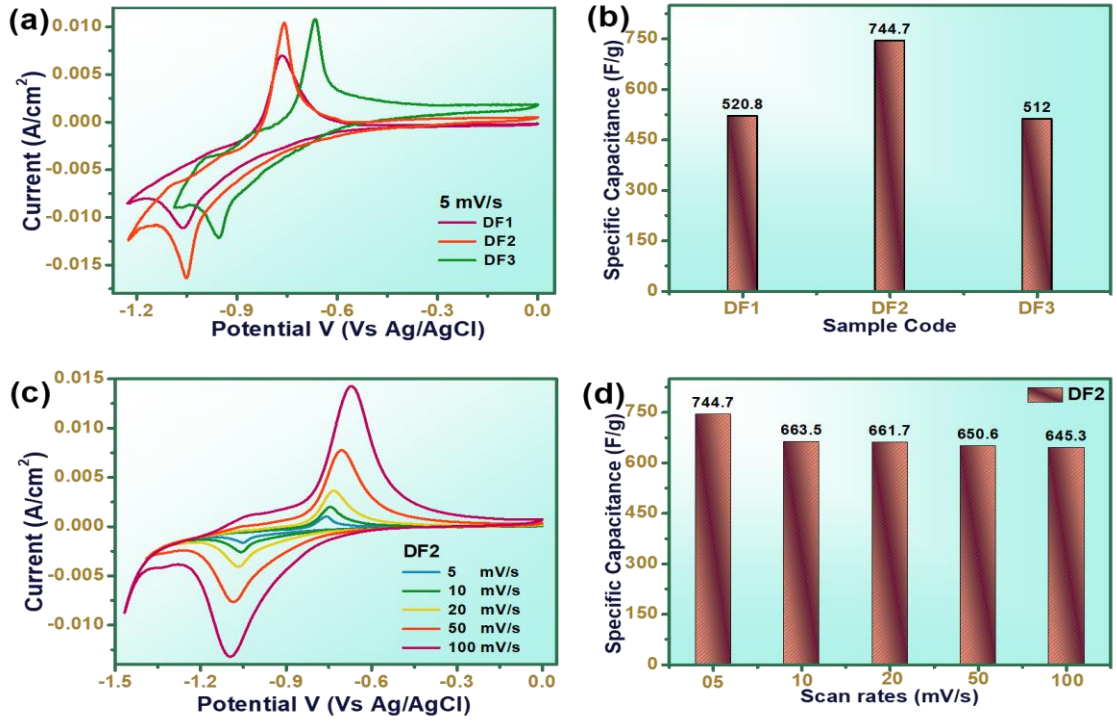


**Fig 5: (a)** CV plots of electrode DF1, DF2, and DF3, **(b)** specific capacitance vs sample code at 5 mV/s, **(c)** CV plots electrode DF2 at sweep rate of 5 -100 mV/s in 1 M KOH, **(d)** specific capacitance vs sweep rate in mV/s of electrode DF2.

| Sample code | Cs in F/g at scan rate of 5 mV/s |
|---|---|
| **DF1** | 520.8 |
| **DF2** | 744.7 |
| **DF3** | 512 |

**Table 2:** Variation of Cs in F/g at scan rate of 5 mV/s for different electrode.

| Scan rate in mV/s | Cs in F/g |
|---|---|
| **05** | 744.7 |

| | |
|---|---|
| **10** | 663.5 |
| **20** | 661.7 |
| **50** | 650.6 |
| **100** | 645.3 |

**Table 3:** Variation of Cs in F/g at different scan rate of DF2 electrode.

| **Material** | **Synthesis method** | **Electrolyte** | **Potential window** | **Cs (F/g)** | **Ref.** |
|---|---|---|---|---|---|
| $Fe_2O_3$ | hydrothermal | 2M KOH | -1.2 - 0 V vs SCE | 558.6 | 2 |
| Fe3O4 | Ultrasonication | 1M Na2SO3 | -0.9 - 0.1 V vs Hg/HgO | 207.7 | 4 |
| FeOOH | Low temperature hydrothermal | 2M KOH | -1.2 - 0 V vs SCE | 714.8 | 5 |
| Bi2WO6 | Sonochemical | 1M KOH | -0.9 - 0.1 V vs Hg/HgO | 304 | 6 |
| MoO2 | Template synthesis | 1M LiOH | -1.2 - -0.5 V vs SCE | 146 | 8 |
| MnFe2O4/G | Hydrothermal | 1M Na2SO4 | -0.8 - 0 V vs Ag/AgCl | 221 | 9 |
| TiN | Hydrothermal | 1M KOH | -1.0 - 0 V vs Ag/AgCl | 123 | 10 |
| $Fe_2O_3$ | SILAR | 1M HOH | -1.47 – 0 V vs Ag/AgCl | 744.7 | **Current working** |

**Table 4**: Comparison of $Fe_2O_3$ electrode with other reported other metal oxide-based thin film in aqueous electrolyte.

***3.5.2 Chronopotentiometry analysis***

The thin film electrodes $Fe_2O_3$ was synthesized using the SILAR method, employing varying Deeping times to produce electrodes denoted as DF1, DF2, and DF3. **Fig. 6 (a)** show the evaluate their electrochemical performance, GCD analyses were conducted at a fixed current density of 1 mA/cm$^2$ in a 1 M KOH electrolyte. The GCD plots revealed specific energy values of 33.1, 75.2, and 44.3 Wh/kg, specific power values of 1.4, 1.3, and 1 kW/kg, and efficiencies of 39.8%, 55.3%, and 49.5% for DF1, DF2, and DF3, respectively show in **Fig. 6 (b)** and all data summarized in **Table 5**. These results demonstrate the superior performance of electrode DF2, characterized by significantly higher specific energy and power values compared to DF1 and DF3. The observed efficiencies reflect the effectiveness of each electrode in storing and releasing electrical energy during charge-discharge cycles

[12][9]. Moreover, the potential window for these measurements ranged from -1.47 to 0 V vs Ag/AgCl, highlighting the electrochemical stability of the $Fe_2O_3$ thin film electrodes.

**Fig. 6 (c)** show the $Fe_2O_3$ thin film electrode DF2 was synthesized using the SILAR method, optimized through Deeping time variation, and evaluated through GCD analysis. The GCD plots for DF2 were found at various current densities of 1-5 mA/cm² in a 1 M KOH electrolyte, revealing specific energy values of 75.2, 31.2, 24.4, 19.2, and 17.3 Wh/kg, respectively. Correspondingly, the specific power values were determined to be 1.3, 2.6, 4, 5.3, and 6.6 kW/kg, with efficiency percentages of 55.3%, 71.7%, 70.4%, 75%, and 61.5%, respectively show in **Fig. 6 (d)**. These results highlight the high SE and SP capabilities of DF2, particularly at lower current densities, where the efficiency is maximized at moderate current densities and slightly decreases at higher densities. The potential window for these measurements was maintained from -1.4 to 0 V vs Ag/AgCl, ensuring an electrochemical stability of the $Fe_2O_3$ electrode [15][22]. The superior performance metrics of DF2, particularly its high SE and SP, combined with notable efficiency, underscore its potential for high-performance energy applications. **Table 6** show the SE, SP, and efficiency of DF2 electrode at different current density.

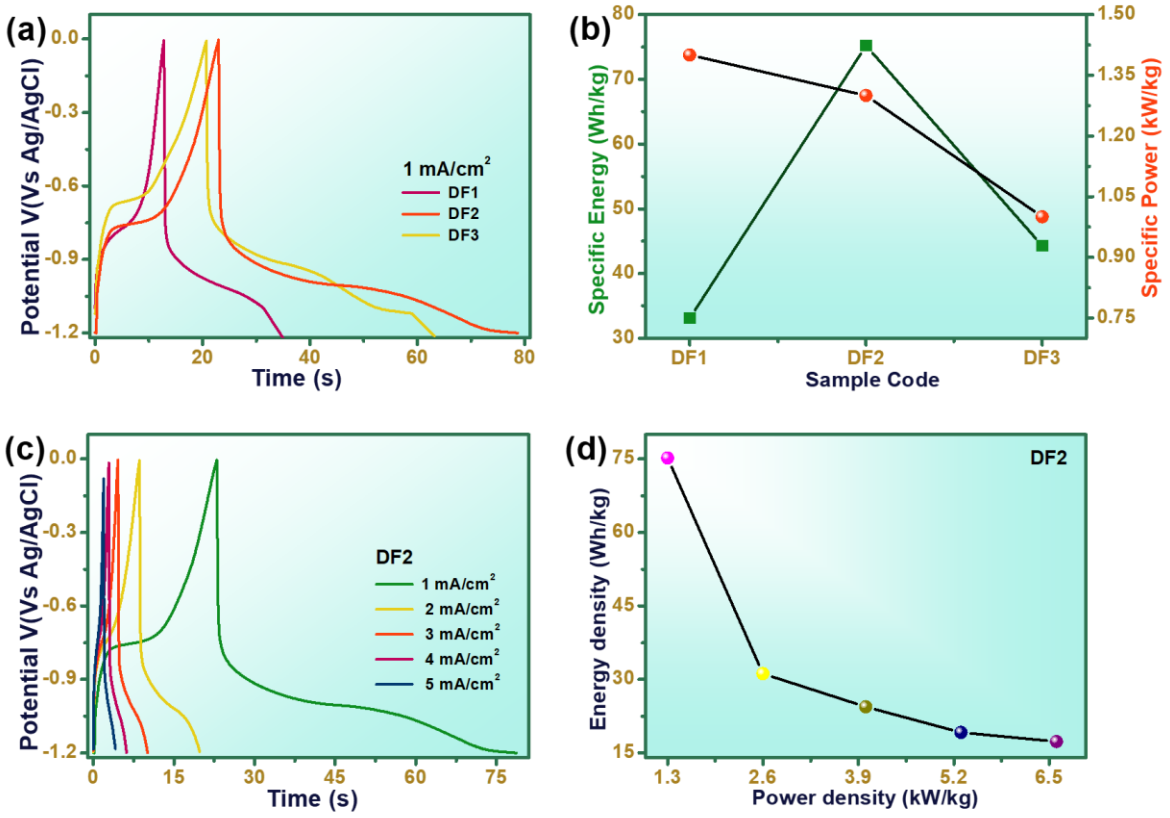


**Fig 6: (a)** The GCD curves of $Fe_2O_3$ at 1 mA/cm$^2$ in 1M KOH electrolyte, **(b)** regon plots of different electrode DF1, DF2, and DF3, **(c)** The GCD plots of electrode DF2 at dissimilar current density from 1-5 mA/cm$^2$ in 1M KOH electrolyte, **(d)** regon plot SE vs SP of electrode DF2.

| Sample code | Specific energy in (Wh/kg) | Specific power in (kW/kg) | Efficiency in (%) |
|---|---|---|---|
| **DF1** | 33.1 | 1.4 | 39.8 |
| **DF2** | 75.2 | 1.3 | 55.3 |
| **DF3** | 44.3 | 1 | 49.5 |

**Table 5:** SE, SP, and efficiency of DF1, DF2, and DF3 electrode

| Current density (mA) | Specific energy in (Wh/kg) | Specific power in (kW/kg) | Efficiency in (%) |
|---|---|---|---|
| **1** | 75.2 | 1.3 | 55.3 |
| **2** | 31.2 | 2.6 | 71.7 |
| **3** | 24.4 | 4 | 70.4 |
| **4** | 19.2 | 5.3 | 75 |
| **5** | 17.3 | 6.6 | 61.5 |

**Table 6:** Specific energy, specific power, and efficiency of DF2 electrode at different current density.

***3.5.3 Electrochemical impedance spectroscopy analysis***

**Fig. 7 (a)** presents a Nyquist plot used to evaluate an internal resistance and capacitive performance of $Fe_2O_3$ electrodes DF1, DF2, and DF3 via EIS in a 1M KOH over a frequency ranging of 100 Hz to 1 MHz. The plot was separated into three distinct regions: the low-frequency area indicating pseudocapacitive behavior, and the high-frequency area showing a charge transfer resistance (Rct) of a Faradaic reaction, represented by a depressed semicircle. The internal resistance (Ri) values were measured to be 1.2 Ω for DF1, 1.5 Ω for DF2, and 2 Ω for DF3. Additionally, the knee frequency, which signifies the highest frequency where capacitive performance is dominant, marks the transition from the semicircular to the linear region in the plot [1][10].

The Nyquist plot for a DF2 electrode, revealed in **Fig. 7 (b)**, includes both the experimental data and the curve fit analyzed using ZsimpWin simulation software. An inset of **Fig. 7 (b)** presents the equivalent circuit for the DF2 electrode, with circuit parameters including a series resistance (Rs) of 1.556 Ω, charge transfer resistance (RCT) of 13.09 Ω, leakage resistance (RL) of 0.4808 Ω, two constant phase elements (CPE) of $1.327\times10^{-3}$ F and $8.79\times10^{-5}$ F, and a Warburg impedance (W) of $1.986\times10^{-3}$ F. Additionally, **Fig. 7 (c)** displays the Bode plot for the DF2 electrode, recorded at open circuit potential (OCP) of -0.4793 V with a 5 mA current in 1M KOH [10] [9][22]. This plot illustrates that as a frequency increases, a phase angle also increases, indicating predominant capacitive performance at the knee frequency. As frequency increases, the phase angle decreases,

signifying a evolution from capacitive to resistive performance. At lower frequencies, the material exhibits capacitive properties, while at higher frequencies, resistive properties dominate. **Fig. 7 (d)** demonstrates a Bode plot for the DF2 electrode, recorded at OCP of -0.7903 V with a 5mA current in a 1 M KOH solution. This plot, which shows the relationship between phase angle and frequency, was crucial for understanding the electrode's characteristics. In a low-frequency range, a phase angle approaches 70°, indicating that the electrode exhibits near-supercapacitive behavior (with a perfect supercapacitor showing a phase angle of 90°) [25] [20].

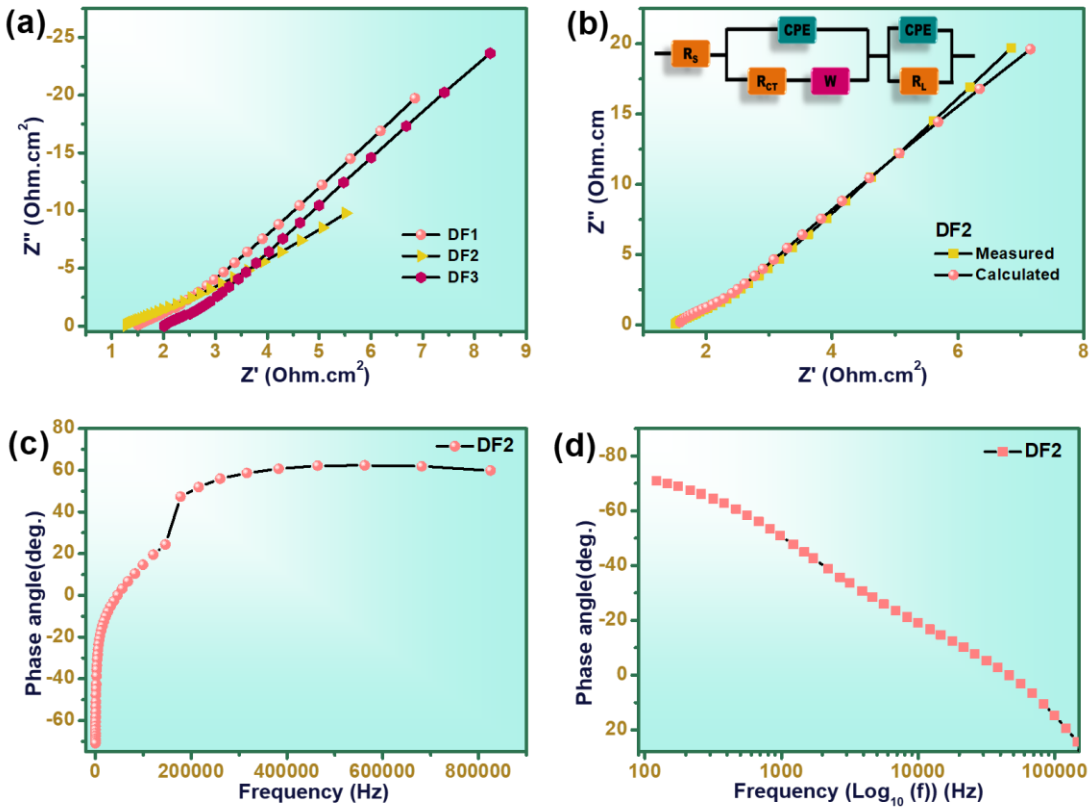


**Fig. 7:** EIS plot of sample electrode $Fe_2O_3$, **(a)** Nyquist plots of electrode DF1, DF2, and DF3, **(b)** nyquist plot & matched nyquist plot with marching circuit of electrode DF2, (c-d) bode plot of electrode DF2.

## 4. Conclusions

we successfully synthesized pure $Fe_2O_3$ electrodes using a simple and consistent one-step SILAR method with varied dipping times. The structural and morphological analysis via XRD and FE-SEM confirmed the hexagonal crystal structure and nanograin-like morphology of the $Fe_2O_3$ electrodes. The electrochemical performance was impressive, with the $Fe_2O_3$ electrode exhibiting a high specific capacitance (Cs) of 744.7 F/g at a scan rate of 5 mV/s. Additionally, the electrode achieved a maximum specific energy (SE) of 75.2 Wh/kg and a specific power (SP) of 1.3 kW/kg at current density of 1 mA/cm². These results designate that the interconnected $Fe_2O_3$ nanospheres suggestively enhance the endurance and performance of supercapacitors. Therefore, $Fe_2O_3$ proves to be a promising material for supercapacitor applications, providing an effective route for future energy storage solutions.

**Institutional Review Board Statement:** Not applicable.

**Informed Consent Statement:** Not applicable.
**Data Availability Statement:** Data will be made available on request.
**Conflicts of Interest:** The authors declare that they have no known competing financial interests or personal relationship that could have appeared to influence the work reported in this paper.

**References**

[1] P. M. Kulal, D. P. Dubal, C. D. Lokhande, and V. J. Fulari, "Chemical synthesis of Fe2O3 thin films for supercapacitor application," *J. Alloys Compd.*, 2011, doi: 10.1016/j.jallcom.2010.11.091.

[2] M. Zhang, K. Chen, X. Chen, X. Peng, X. Sun, and D. Xue, "Ethylenediamine-assisted crystallization of Fe2O3 microspindles with controllable size and their pseudocapacitance performance," *CrystEngComm*, 2015, doi: 10.1039/c4ce02417f.

[3] N. C. Maile *et al.*, "Capacitive property studies of inexpensive SILAR synthesized polyaniline thin films for supercapacitor application," *SN Appl. Sci.*, 2019, doi: 10.1007/s42452-019-1403-6.

[4] V. B. Suryavanshi, R. G. Bobade, B. J. Lokhande, and R. C. Ambare, "Electro-Synthesized Bismuth Oxide Nanomaterials on Flexible Substrate Electrode for Supercapacitor Application," *ES Energy Environ.*, 2023, doi: 10.30919/esee944.

[5] L. Wang, H. Ji, S. Wang, L. Kong, X. Jiang, and G. Yang, "Preparation of Fe3O4 with high specific surface area and improved capacitance as a supercapacitor," *Nanoscale*, 2013, doi: 10.1039/c3nr00256j.

[6] R. G. Bobade *et al.*, "Concentration-dependent SILAR synthesized Di-bismuth copper oxide nano-materials electrode in asymmetric supercapacitor," *J. Mater. Sci. Mater. Electron.*, vol. 35, no. 2, p. 129, Jan. 2024, doi: 10.1007/s10854-023-11818-4.

[7] D. S. et al. Suryawanshi, V.B., Bobade, R.G., Gaikwad, "Nano-architectured BaO thin film electrode synthesized via SILAR technique for supercapacitor application.," *Chem. Pap.*, 2024, doi: https://doi.org/10.1007/s11696-024-03400-x.

[8] D. S. Gaikwad *et al.*, "SILAR-synthesized Co3O4/Bi2O3 on copper substrate nanocomposite electrode and asymmetric Co3O4/Bi2O3/CuO: AC solid-state device in supercapacitor," *J. Mater. Sci. Mater. Electron.*, 2024, doi: 10.1007/s10854-024-12220-4.

[9] R. G. Bobade *et al.*, "Influence of Deposition Potential on Electrodeposited Bismuth-Copper Oxide Electrodes for Asymmetric Supercapacitor," *Batter. Supercaps*, 2024, doi: 10.1002/batt.202400163.

[10] R. G. Bobade, U. T. Nakate, P. Roasiah, M. Ouladsmane, B. J. Lokhande, and R. C. Ambare, "Nanoarchitectonics of Bi2CuO4 electrodes for asymmetric Bi2CuO4//AC solid-state device in supercapacitor application," *Inorg. Chem. Commun.*, vol. 154, p. 110998, Aug. 2023, doi: 10.1016/j.inoche.2023.110998.

[11] S. G. Randive, R. G. Bobade, R. C. Ambare, and B. J. Lokhande, "Spray pyrolyzed thorn-like nanostructured nickel oxide electrodes for symmetric supercapacitor device," *J. Mater. Sci. Mater. Electron.*, 2024, doi: 10.1007/s10854-024-12229-9.

[12] K. Chen, X. Chen, and D. Xue, "Hydrothermal route to crystallization of FeOOH nanorods via FeCl 3 ·6H 2 O: effect of Fe 3+ concentration on pseudocapacitance of

iron-based materials," *CrystEngComm*, vol. 17, no. 9, pp. 1906–1910, 2015, doi: 10.1039/C4CE02504K.

[13] V. D. Nithya, R. K. Selvan, D. Kalpan, L. Vasylechko, and C. Sanjeeviraj, "Synthesis of Bi2WO6 nanoparticles and its electrochemical propertiesin different electrolytes for pseudocapacitor electrodes," *Electrochim. Acta*, 2013, doi: 10.1016/j.electacta.2013.07.138.

[14] S. S. Raut and B. R. Sankapal, "Comparative studies on MWCNTs, Fe2O3 and Fe2O3/MWCNTs thin films towards supercapacitor application," *New J. Chem.*, 2016, doi: 10.1039/c5nj03628c.

[15] E. C. Wheeler-Jones, M. J. Loveridge, and A. J. Roberts, "High Power Energy Storage: New Materials for Large Format Supercapacitors," *ECS Meet. Abstr.*, 2019, doi: 10.1149/ma2019-04/5/267.

[16] B. Li, Y. Fu, H. Xia, and X. Wang, "High-performance asymmetric supercapacitors based on MnFe2O 4/graphene nanocomposite as anode material," *Mater. Lett.*, 2014, doi: 10.1016/j.matlet.2014.02.046.

[17] X. Lu *et al.*, "Stabilized TiN nanowire arrays for high-performance and flexible supercapacitors," *Nano Lett.*, 2012, doi: 10.1021/nl302761z.

[18] B. J. Lokhande, R. C. Ambare, and S. R. Bharadwaj, "Thermal optimization and supercapacitive application of electrodeposited Fe2O3 thin films," *Meas. J. Int. Meas. Confed.*, 2014, doi: 10.1016/j.measurement.2013.09.005.

[19] S. N. Khatavkar and S. D. Sartale, "α-Fe2O3 thin films by liquid phase deposition: low-cost option for supercapacitor," *J. Solid State Electrochem.*, vol. 21, no. 9, pp. 2555–2566, Sep. 2017, doi: 10.1007/s10008-016-3457-3.

[20] D. S. Gaikwad *et al.*, "Electrochemical property of nanosphere-like MgO electrode synthesized via SILAR in asymmetric supercapacitor," *J. Mater. Sci. Mater. Electron.*, 2024, doi: 10.1007/s10854-024-12196-1.

[21] C. Xia, C. Hu, Y. Xiong, and N. Wang, "Synthesis of α-Fe2O3 hexagons and their magnetic properties," *J. Alloys Compd.*, 2009, doi: 10.1016/j.jallcom.2009.02.106.

[22] R. G. Bobade, N. B. Dabke, S. F. Shaikh, B. J. Lokhande, R. S. Mane, and R. C. Ambare, "Facile chemical synthesis of BaO:MgO nanorods for designing distinctive solid-state asymmetric supercapacitor device with activated carbon," *J. Energy Storage*, vol. 84, p. 110776, Apr. 2024, doi: 10.1016/j.est.2024.110776.

[23] M. Aalim, I. Irshad, A. M. Tantray, A. Sohail, B. Want, and M. A. Shah, "Effect of chromium (Cr)-doping on electrochemical performance of microwave synthesized hematite (α-CrxFe2−xO3) nanosheets for supercapacitor application," *J. Mater. Sci. Mater. Electron.*, 2023, doi: 10.1007/s10854-023-10825-9.

[24] P. J. Sephra, P. Baraneedharan, M. Sivakumar, T. D. Thangadurai, and K. Nehru, "In situ growth of hexagonal-shaped α-Fe2O3 nanostructures over few layered graphene by hydrothermal method and their electrochemical performance," *J. Mater. Sci. Mater. Electron.*, 2018, doi: 10.1007/s10854-018-8676-1.

[25] B. Pandit *et al.*, "One-pot hydrothermal preparation of hierarchical manganese oxide nanorods for high-performance symmetric supercapacitors," *J. Energy Chem.*, vol. 65, pp. 116–126, Feb. 2022, doi: 10.1016/j.jechem.2021.05.028.